J. Plasma Phys. (2022), *vol*. 88, 905880301
Published by Cambridge University Press

doi:10.1017/S0022377822000356

Implications of weak rippling of the shock ramp on the pattern of the electromagnetic field and ion distributions

Michael Gedalin [1],† **and Natalia Ganushkina** [2]

[1]Department of Physics, Ben-Gurion University of the Negev, Beer-Sheva, Israel

[2]Finnish Meteorological Institute, Helsinki, Finland

(Received 27 February 2022; revised 15 April 2022; accepted 19 April 2022)

Collisionless shocks undergo structural changes with the increase of Mach number. Observations and numerical simulations indicate development of time-dependent rippling. It is not known at present what causes the rippling. However, effects of such rippling on the field pattern and ion motion and distributions can be studied without precise knowledge of the causes and detailed shape. It is shown that deviations of the normal component of the magnetic field from the constant value indicate certain spatial dependence of the rippling. Deviations of the motional electric field from the constant value indicate time dependence. It is argued that whistler waves should propagate towards upstream and downstream regions from the rippled ramp. It is shown that the downstream pattern of the fields and ion distributions should follow the rippling pattern, while collisionless relaxation should be faster than in the stationary planar case.

Key words: space plasma physics, astrophysical plasmas

1. Introduction

Collisionless shocks are among the most fundamental strongly nonlinear phenomena in space plasmas. The unfading interest regarding collisionless shocks and the ongoing research during the last six decades is determined by the fact the these shocks are the most efficient accelerators of charged particles in plasmas (Axford, Leer & Skadron 1977; Krymskii 1977; Bell 1978; Blandford & Ostriker 1978; Vasilev, Toptygin & Chirkov 1978; Toptyghin 1980; Jokipii 1982; Drury 1983; Blandford & Eichler 1987). The highest energies are achieved at supernova remnant (SNR) shocks (Vink 2020). Acceleration processes depend on the shock structure, which makes understanding of the latter the key issue in shock physics. All information about the SNR shocks is obtained remotely via the electromagnetic emission coming from the particles which are heated and accelerated by the shocks. *In situ* observations of collisionless shocks are possible only in the heliosphere. Supernova remnant shocks are believed to be high-Mach number shocks (Reynolds 2004; Vink 2004*b*, *a*; Jones 2011; Raymond 2018). Heliospheric shocks with

† Email address for correspondence: gedalin@bgu.ac.il

Mach numbers possibly approaching the Mach numbers of SNR shocks are observed at outer planets (Masters *et al.* 2013; Sulaiman *et al.* 2015; Madanian *et al.* 2021). Most shock observations have been and are being performed at the Earth bow shock. As a result of these observations and theory development, it seems that at present the structure of low-Mach-number shocks is thoroughly studied observationally and understood rather well (Greenstadt *et al.* 1980; Russell *et al.* 1982; Mellott & Greenstadt 1984; Jones & Ellison 1987; Gosling, Winske & Thomsen 1988; Farris, Russell & Thomsen 1993; Gedalin 1996*b*; Balikhin *et al.* 2008; Gedalin, Friedman & Balikhin 2015; Gedalin *et al.* 2022) (see, however, Wilson *et al.* (2017)). With the increase of Mach number the shock front undergoes structural changes, developing rippling and time dependence (Bale *et al.* 2005; Moullard *et al.* 2006; Lobzin *et al.* 2008; Krasnoselskikh *et al.* 2013; Burgess *et al.* 2016; Hao *et al.* 2016). These changes do not appear abruptly when the Mach number exceeds some critical value but gradually become more and more pronounced when the Mach number increases (Ofman & Gedalin 2013). Rippling and time dependence (reformation), as well as generation of the propagating upstream whistlers (Wilson *et al.* 2009; Hull *et al.* 2012; Ramírez Vélez *et al.* 2012; Wilson *et al.* 2012, 2017) may be interrelated (Burgess *et al.* 2016; Gingell *et al.* 2017; Umeda & Daicho 2018; Omidi *et al.* 2021). At present, it is not quite clear what causes rippling. One of the plausible explanations is an instability of the waves propagating along the shock surface (Lowe & Burgess 2003; Burgess & Scholer 2007; Burgess *et al.* 2016). Such surface modulations should affect the processes at the shock front, among them ion reflection (Johlander *et al.* 2016, 2018). In this paper we study the implications of weak time-dependent rippling on the shock ramp and the adjacent upstream and downstream regions. We propose an analytical model of the magnetic and electric fields inside a weakly rippled shock transition layer, and analyse the consequences which can be verified with numerical simulations and applied to observations to estimate the rippling parameters.

2. Weak non-stationary rippling: a model

In the absence of a good theory we model rippling as spatial and temporal dependence localized within the ramp. We start with a monotonic magnetic profile of a low-Mach-number shock ramp which we model using the following expressions (Gedalin *et al.* 2015):

$$\frac{B_z}{B_u \sin\theta} = \frac{R+1}{2} + \frac{R-1}{2}\tanh\frac{3x}{D}, \tag{2.1}$$

$$B_x = B_u \cos\theta, \tag{2.2}$$

$$B_y = k_B \frac{\mathrm{d}B_z}{\mathrm{d}x}, \tag{2.3}$$

$$E_y = V_u B_u \sin\theta, \quad E_z = 0, \tag{2.4a,b}$$

$$E_x = -\frac{\mathrm{d}\phi_{\mathrm{NIF}}}{\mathrm{d}x} = -k_E \frac{\mathrm{d}B_z}{\mathrm{d}x}. \tag{2.5}$$

Here, subscript u refers to the upstream region, θ is the angle between the shock normal and the upstream magnetic field vector, B_u is the upstream magnetic field magnitude, E_y is the motional electric field, E_x is the cross-shock electric field, B_y is the non-coplanar component of the magnetic field, D is the ramp width and R is the ratio of the downstream to upstream B_z. The shock normal is along the x-direction and the non-coplanarity direction is y. The analysis is done in the normal incidence frame (NIF), where the

https://doi.org/10.1017/S0022377822000356 Published online by Cambridge University Press

upstream plasma flow is along the shock normal. The coefficients k_E, k_B are obtained from

$$-\int E_x \,\mathrm{d}x = \phi_{\mathrm{NIF}} \equiv s_{\mathrm{NIF}}(m_p V_u^2/2e), \tag{2.6}$$

$$-\int (E_x + V_u \tan\theta B_y)\,\mathrm{d}x = \phi_{HT} \equiv s_{HT}(m_p V_u^2/2e), \tag{2.7}$$

where ϕ_{NIF} and ϕ_{HT} are the cross-shock potentials in the NIF and the de Hoffman–Teller frame (HT), respectively. In the HT frame the upstream plasma flow is along the upstream magnetic field. The relations for B_y and E_x are approximations derived from the two-fluid plasma model for low-Mach-number shocks, both subcritical and supercritical (Goodrich & Scudder 1984; Gosling *et al.* 1988; Gedalin 1996*b*). Within this approximation $k_B = c\cos\theta/M\omega_{pi}$ is the whistler length. Here, $M = V_u/V_A$ is the Alfvén Mach number, c/ω_{pi} is the ion inertial length, $\omega_p = \sqrt{4\pi n_u e^2/m_p}$, $V_A = B_u/\sqrt{4\pi n_u m_p}$ is the Alfvén speed, n_u is the upstream proton number density and m_p is the proton mass. For simplicity, the plasma is assumed to consist of protons and electrons only. For brevity, in what follows we write down expressions for the fields using $c \equiv 1$. The speed of light may be easily restored at the end using dimension arguments. Let us introduce the vector and scalar potentials, as follows:

$$A_y = A(x) + B_u\cos\theta z - V_u B_u \sin\theta t, \tag{2.8}$$

$$A_z = k_B \frac{\mathrm{d}A}{\mathrm{d}x}, \tag{2.9}$$

$$\phi = k_E \frac{\mathrm{d}A}{\mathrm{d}x}, \tag{2.10}$$

so that

$$B_z = \frac{\partial A_y}{\partial x}, \tag{2.11}$$

$$B_x = \frac{\partial A_y}{\partial z} = B_u\cos\theta, \tag{2.12}$$

$$B_y = -\frac{\partial A_z}{\partial x}, \tag{2.13}$$

$$E_x = -\frac{\partial \phi}{\partial x}, \tag{2.14}$$

$$E_y = -\frac{\partial A_y}{\partial t} = V_u B_u \sin\theta, \tag{2.15}$$

$$E_z = -\frac{\partial A_z}{\partial t} = 0. \tag{2.16}$$

Let us now introduce rippling, as follows. Let $X = x + f$, $f(x, y, z, t) = a\psi(y, z, t)g(x)$, $g(x \to \pm\infty) = 0$, $(\mathrm{d}g/\mathrm{d}x)(x \to \pm\infty) = 0$, where a is the amplitude (dimensions of length), while ψ and g are dimensionless. Consider a vector potential and a scalar potential

$$A_y = A(X) + B_u\cos\theta z - V_u B_u \sin\theta t, \tag{2.17}$$

$$A_z = k_B \frac{\partial A}{\partial X}, \tag{2.18}$$

https://doi.org/10.1017/S0022377822000356 Published online by Cambridge University Press

$$\phi = k_E \frac{\partial A}{\partial X}. \tag{2.19}$$

Note that it is always possible to choose the gauge where one of $\boldsymbol{A}$ components vanishes. The fields are now

$$B_z = B_u \sin\theta B(1 + f_x), \tag{2.20}$$

$$B_x = B_u \sin\theta \left(\cot\theta - Bf_z + k_B B_X f_y\right), \tag{2.21}$$

$$B_y = -k_B B_u \sin\theta B_X(1 + f_x), \tag{2.22}$$

$$E_x = -k_E B_u \sin\theta B_X(1 + f_x), \tag{2.23}$$

$$E_y = V_u B_u \sin\theta - B_u \sin\theta B f_t - k_E B_u \sin\theta B_X f_y, \tag{2.24}$$

$$E_z = -B_u \sin\theta k_B B_X f_t - k_E B_u \sin\theta B_X f_z. \tag{2.25}$$

The details of the derivation and the definitions of B_X, f_t, f_x, f_y and f_z are given in the Appendix (A).

3. Implications for the fields in the ramp

In what follows we analyse what could be the signatures of the weak rippling in observations and simulations. In the first order on derivatives $f_t, f_x, f_y, f_z, f_{xx}$ one has

$$\frac{\partial B_z}{\partial x} = B_u \sin\theta \left(B_X(1 + 2f_x) + Bf_{xx}\right), \tag{3.1}$$

$$\frac{\partial B_z}{\partial y} = B_u \sin\theta B_X f_y, \tag{3.2}$$

$$\frac{\partial B_x}{\partial y} = \frac{\partial B_x}{\partial z} = 0, \tag{3.3}$$

$$\frac{\partial B_y}{\partial x} = -k_B B_u \sin\theta \left(B_{XX}(1 + 2f_x) + B_X f_{xx}\right), \tag{3.4}$$

$$\frac{\partial B_y}{\partial z} = -k_B B_u \sin\theta B_{XX} f_z. \tag{3.5}$$

The most notable distinction from the stationary planar shock is that B_x and E_y are no longer constant throughout the ramp, and $E_z \neq 0$. If k_B is also small, the major deviations are

$$\delta B_x \approx -B_u \sin\theta B f_z, \tag{3.6}$$

$$\delta E_y \approx -B_u \sin\theta B f_t - k_E B_u \sin\theta B_X f_y, \tag{3.7}$$

$$\delta E_z \approx -k_E B_u \sin\theta B_X f_z. \tag{3.8}$$

As an example, consider ripples localized within the ramp and propagating along the shock front, of the form $\psi = \sin(k_y y + k_z z - \omega t)$. Then there is no phase difference between δB_x, δE_y and δE_z, and

$$\delta E_y = -\frac{\omega}{k_z}\delta B_x + \frac{k_z}{k_y}\delta E_z, \tag{3.9}$$

$$\frac{\delta E_z}{\delta B_x} = k_E \frac{B_X}{B}. \tag{3.10}$$

https://doi.org/10.1017/S0022377822000356 Published online by Cambridge University Press

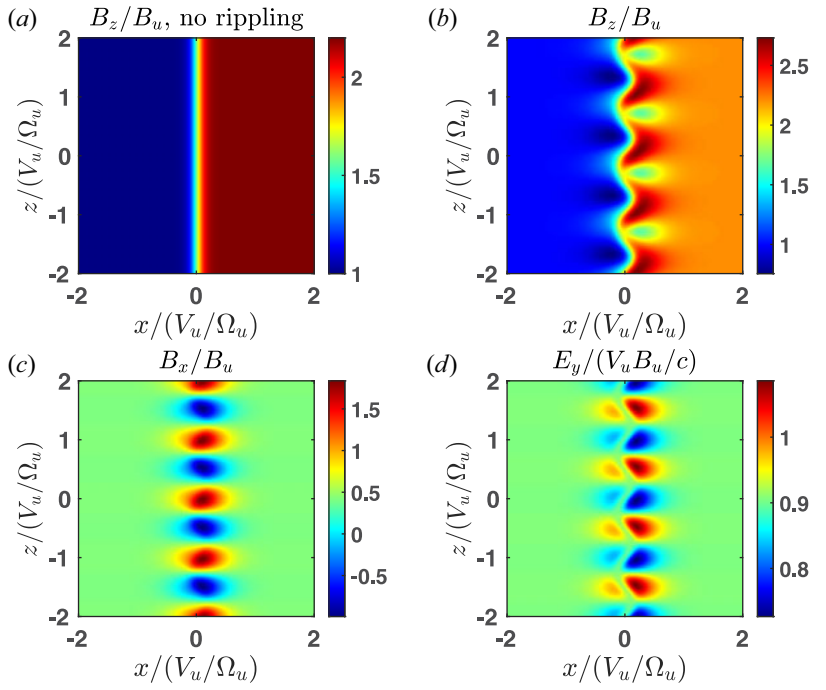

FIGURE 1. A visual comparison of the main magnetic component (*a*) B_z for a stationary planar shock, (*b*) B_z for a rippled shock, (*c*) B_x for a rippled shock and (*d*) E_y for a rippled shock. Parameters are given in text.

Figure 1 illustrates the effect of rippling on the components of the fields. Figure 1(*a*,*b*) provides a visual comparison of the main magnetic component B_z for a stationary shock and its rippled counterpart. Figure 1(*c*,*d*) shows the field components for which the effect is especially pronounced. For this visualization the following parameters were used: $M = 2.5$, $\theta = 65^\circ$, $B_d/B_u = 2.2$, $s_{\mathrm{NIF}} = 0.5$, $s_{HT} = 0.1$, $D = c/\omega_{pi}$, $k_zV_u/\Omega_u = 2\pi$, $k_yV_u/\Omega_u = \pi/2$, $\omega = \Omega_u$, $a = 0.3(c/\omega_{pi})$, where $\Omega_u = eB_u/m_pc$ and $(B_d/B_u)^2 = R^2\sin^2\theta + \cos^2\theta$. The localizing function is $g(x) = \cosh^{-2}(x/D)$. The rippling amplitude, a and the wavelength along the z direction $2\pi/k_z$ are taken to be similar to what was found numerically by Ofman & Gedalin (2013), albeit for slightly higher Mach numbers. The profiles are shown for $y = 0$ and $t = 0$. Note that the rippling amplitude is rather small but the effect is quite noticeable, especially in the components B_x and E_y. Thus, even if rippling may be difficult to recognize by the main magnetic component or the magnetic field magnitude, the two mentioned components easily disclose non-planarity and/or time dependence. For the chosen model of rippling B_x deviates from the constant value mainly because of the spatial dependence on z, while E_y deviates from the constant value due to the temporal dependence and the spatial dependence on y. Figure 1(*c*,*d*) suggest that the rippling parameters can be estimated from observations by comparing the variations of the components of the fields. For example, $\delta E_y + (\omega/k_z)\delta B_x$ and δB_x seem to not overlap, which suggests that minimization of $\int(\delta E_y + \lambda\delta B_x)\delta B_x\,\mathrm{d}x$, where λ is a variable parameter, may provide an estimate of ω/k_z.

There is an overshoot with $\max(|B|/B_u) = 2.73$, and the magnetic field magnitude drops to below the upstream value, $\min(|B|/B_u) = 0.76$. The normal component of the magnetic field varies in the range $-0.99 \le B_x/B_u < 1.84$ while without rippling one has

https://doi.org/10.1017/S0022377822000356 Published online by Cambridge University Press

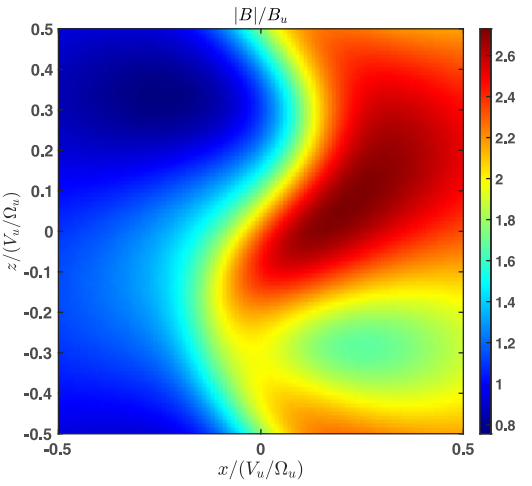

FIGURE 2. Close-up on the magnetic field magnitude illustrating changes of the local normal direction along the rippled shock front.

$B_x/B_u = 0.42$. For all practical purposes the local normal can be defined as the direction of $\nabla|\boldsymbol{B}|$ in the region where the magnitude of the gradient is maximum. For the chosen model rippled profile the deviations of this direction from $\hat{x}$ reach values $> 30^\circ$, as can be seen from figure 2. Thus, for a weakly rippled shock the observational determination of the shock normal using magnetic coplanarity or minimum variance might have a $\pm 30^\circ$ error depending on the spacecraft trajectory across the shock.

Shocks which exhibit rippling typically have overshoots. An overshoot is not included in (2.1) and in the visualization. The generality of the expressions, however, is limited only by the model (2.17)–(2.19). An overshoot can be easily incorporated in the model profile, for example, as in Gedalin, Pogorelov & Roytershteyn (2021).

4. Implications for upstream and downstream waves close to the ramp

The rippled ramp is acting as a boundary which is perturbed according to $\psi = \sin(k_y y + k_z z - \omega t)$. These boundary perturbations should generate waves propagating towards upstream and downstream. The only low-frequency electromagnetic wave which can propagate towards upstream is the whistler wave which has the Doppler shifted dispersion relation

$$\tilde{\omega} = \omega - k_x V_u = \frac{\sqrt{k_x^2 + k_y^2 + k_z^2}(k_x \cos\theta + k_z \sin\theta)}{\omega_{pi}} v_A, \tag{4.1}$$

where $\tilde{\omega}$ is the whistler frequency in the frame of the upstream plasma flow and $k_x < 0$. The relation (4.1) determines k_x. Note that for $k_y = k_z = 0$ and $\omega = 0$ this relation reduces to the phase-standing whistler for a planar stationary shock. In this interpretation the time-dependent rippled shock surface is the source of the whistlers propagating into the upstream region. The inverse should be also true: if whistlers are constantly escaping from the shock front they should leave a corresponding imprint at the front itself. Thus, the rippling pattern at the shock front and the whistler pattern in the upstream region can be expected to be mutually consistent. For the upstream whistler $\cos\theta_{\boldsymbol{k},\hat{n}} = |k_x|/k$ and $\cos\theta_{\boldsymbol{k},\boldsymbol{B}_u} = (k_x \cos\theta + k_z \sin\theta)/k$, where $\theta_{\boldsymbol{k},\hat{n}}$ and $\theta_{\boldsymbol{k},\boldsymbol{B}_u}$ are the angles between the

https://doi.org/10.1017/S0022377822000356 Published online by Cambridge University Press

propagation direction of the whistler and the shock normal and the upstream magnetic field, respectively. For the parameters chosen for the above visualization $k_x V_u/\Omega_u \approx -3.86$, $\theta_{\boldsymbol{k},\hat{n}} \approx 57^\circ$, $\theta_{\boldsymbol{k},\boldsymbol{B}_u} \approx 57^\circ$.

In the downstream region the dispersion relation for the whistler changes accordingly,

$$\omega - k_{d,x}V_{d,x} - k_z V_{d,z} = \frac{\sqrt{k_{d,x}^2 + k_y^2 + k_z^2}(k_{d,x}\cos\theta_d + k_z \sin\theta_d)}{\omega_{pi,d}} v_{A,d}, \tag{4.2}$$

where $V_{d,x}$ and $V_{d,z}$ are the components of the downstream flow velocity, θ_d is the angle between the shock normal and the downstream magnetic field, $\omega_{pi,d}$ is the ion plasma frequency calculated with the downstream ion density and $v_{A,d}$ is the Alfvén speed in the downstream region. Note that in the downstream region waves propagate from the ramp into the downstream and the corresponding $k_{d,x} > 0$. In numerical simulations capable of resolving whistlers two sets of fronts would be observed diverging from the ramp (Yuan *et al.* 2009; Riquelme & Spitkovsky 2011). If whistler waves are not resolved properly, small pieces of such diverging fronts may be still observed. Diverging waves should remove energy from the ramp, thus providing an additional channel of the redistribution of the energy of the directed flow of the incident ions. The amplitude of the diverging waves and the amplitude of the rippling depend on the mechanism which causes rippling and further sustains it. This mechanism is not known at present and is the subject of intensive studies (Lowe & Burgess 2003; Burgess & Scholer 2007; Johlander *et al.* 2016, 2018; Omidi *et al.* 2021).

5. Two-fluid hydrodynamics within the rippled shock

The two-fluid approach was used in attempts to describe the shock front of a laminar (low Mach number, low β) oblique shock (see, e.g. Gedalin 1998). Although a shock-like profile was not obtained, some useful estimates of the scales were derived. Here we outline a semiquantitative extension of the two-fluid description with the above modelled rippling. The two-fluid model has to be adapted separately to the different conditions inside the ramp and downstream of the ramp. There are no changes in the upstream region in comparison with the standard description (Gedalin 1998). The ramp width is substantially smaller than the ion convective gyroradius in supercritical and even laminar subcritical shocks (Russell *et al.* 1982; Mellott & Greenstadt 1984; Farris *et al.* 1993; Newbury & Russell 1996; Bale *et al.* 2005; Hobara *et al.* 2010; Krasnoselskikh *et al.* 2013). Therefore, it is more appropriate to treat the ions kinetically. The collisionless Vlasov equation which simply states that the distribution function is constant along the particle trajectory, $f_i(\boldsymbol{r}_i, \boldsymbol{v}_i, t) = f_0(\boldsymbol{r}_0, \boldsymbol{v}_0, t_0)$, where $\boldsymbol{r}_i$ and $\boldsymbol{v}_i$ are the solutions of the equations of motion

$$\frac{\mathrm{d}\boldsymbol{r}_i}{\mathrm{d}t} = \boldsymbol{v}_i, \quad \frac{\mathrm{d}\boldsymbol{v}_i}{\mathrm{d}t} = \frac{e}{m_p}\left(\boldsymbol{E} + \frac{\boldsymbol{v}_i}{c} \times \boldsymbol{B}\right), \tag{5.1a,b}$$

with the initial conditions $\boldsymbol{r}_i(t = t_0) = \boldsymbol{r}_0$, $\boldsymbol{v}_i(t = t_0) = \boldsymbol{v}_0$. The equations of motion inside the ramp are not integrable even in the stationary planar case. It was shown that a reasonable solution can be derived in the following approximation: (*a*) the ramp is narrow; and (*b*) the ratio of the upstream thermal speed to the flow speed is small, $v_{iT}/V_u \ll 1$ (Gedalin 1997, 2021). Here $v_{iT} = \sqrt{T_u/m_p}$, T_u being the temperature of the incident ion distribution. In this approximation

$$V_{i,x} = \sqrt{V_u^2 - 2e\phi_{\mathrm{NIF}}/m_m}, \quad V_{i,y} = V_{i,z} = 0, \tag{5.2a,b}$$

https://doi.org/10.1017/S0022377822000356 Published online by Cambridge University Press

$$n_i = \frac{n_u V_u}{\sqrt{V_u^2 - 2e\phi_{\rm NIF}/m_p}}, \tag{5.3}$$

where n_i is the ion number density and $\boldsymbol{V}_i$ is the bulk (hydrodynamical) velocity of the ions. The main effect is the deceleration by the cross-shock electric field as given by (5.2*a*,*b*)–(5.3).

The electron velocity $\boldsymbol{V}_e$ can be obtained from

$$\frac{4\pi en}{c}(\boldsymbol{v} - \boldsymbol{V}_e) = \boldsymbol{\nabla} \times \boldsymbol{B}, \tag{5.4}$$

where quasineutrality $n_i = n_e = n$ is assumed. Neglecting ion velocity in the y and z directions inside the ramp one has

$$V_{ex} = V_{i,x} - \frac{B_u \sin\theta}{4\pi ne}\left(B_X f_y + k_B B_{XX} f_z\right), \tag{5.5}$$

$$V_{ey} = \frac{B_u \sin\theta}{4\pi ne}\left(B_X(1 + 2f_x) + B f_{xx}\right), \tag{5.6}$$

$$V_{ez} = \frac{B_u \sin\theta}{4\pi ne}\left(k_B B_{XX}(1 + 2f_x) + k_B B_X f_{xx}\right), \tag{5.7}$$

where $V_x = \sqrt{V_u^2 - 2e\phi/m}$ and we restricted ourselves with the lowest and first order only. In the lowest order the electron velocity is

$$V_{ex}^{(0)} = V_{i,x}, \tag{5.8}$$

$$V_{ey}^{(0)} = \frac{cB_u \sin\theta}{4\pi ne} B_X, \tag{5.9}$$

$$V_{ez}^{(0)} = \frac{cB_u \sin\theta}{4\pi ne} k_B B_{XX}, \tag{5.10}$$

as in the stationary planar case. In the approximation of massless cold electrons one has $\boldsymbol{E} + \boldsymbol{V}_e \times \boldsymbol{B}/c = 0$ which eventually gives

$$\frac{e}{m_p}\left(\frac{{\rm d}\phi_{\rm NIF}}{{\rm d}X}\right)\frac{n_u V_u}{\sqrt{V_u^2 - 2e\phi_{\rm NIF}/m_p}} = \frac{1}{8\pi m_p}\frac{\rm d}{{\rm d}X}B^2, \tag{5.11}$$

$$V_u - V_{i,x} = \frac{B^2 - B_u^2}{8\pi n_u V_u m_p}, \tag{5.12}$$

$$\frac{V_{i,x}}{V_u} = 1 - \frac{b^2 - 1}{2M^2}, \quad b = B/B_u, \tag{5.13}$$

$$1 - \frac{n_u}{n_i} = \frac{b^2 - 1}{2M^2} \to 1 + \frac{1}{2M^2} = \frac{V_{i,x}}{V_u} + \frac{b^2}{2M^2}. \tag{5.14}$$

This expressions are identical to the expressions obtained for the stationary planar shock with the only replacement $x \to X$ (Gedalin 2021). The above means that in the lowest-order approximation the ramp structure and the ion velocity remain the same as in the stationary planar case, only the position of the ramp edges depend on y, z, t. This has important implications for the ion motion and the ion distribution just behind the ramp.

https://doi.org/10.1017/S0022377822000356 Published online by Cambridge University Press

The main correction to the electron velocity due to the rippling is that $V_{ex} \neq V_x$, which probably may be observable in spacecraft measurements. In a quasi-perpendicular shock, where k_B is small, this velocity difference is directly related to the spatial variations in the y direction. For simplicity, we write down the expression $\boldsymbol{E} + \boldsymbol{V}_e \times \boldsymbol{B}/c = 0$ for $\cos\theta = 0$ and $k_B = 0$ as

$$-k_E B_X(1 + f_x) + \frac{B_u}{4\pi ne} B\left(B_X(1 + 3f_x) + Bf_{xx}\right) = 0, \tag{5.15}$$

$$V_u - Bf_t - k_E B_X f_y - B\left(V_x - \frac{B_u}{4\pi ne}\left(B_X f_y + k_B B_{XX} f_z\right)\right) = 0, \tag{5.16}$$

$$-k_E B_X f_z - \frac{B_u}{4\pi ne} B B_X f_z = 0. \tag{5.17}$$

In the lowest order we have

$$-k_E + \frac{B_u}{4\pi ne} B = 0, \quad V_u - V_{i,x} B = 0. \tag{5.18a,b}$$

Both mean $n/B = \text{const.}$, as should occur in a perpendicular shock. The first-order corrections add the following constraints:

$$-k_E B_X f_x + \frac{B_u}{4\pi ne} B\left(3B_X f_x\right) + Bf_{xx}) = 0, \tag{5.19}$$

$$-Bf_t - k_E B_X f_y + B\frac{B_u}{4\pi ne}\left(B_X f_y + k_B B_{XX} f_z\right) = 0. \tag{5.20}$$

For $f = g(x)\sin(k_y y + k_z z - \omega t)$ the equations take the form

$$-k_E B_X g_x + \frac{B_u}{4\pi ne} B\left(3B_X g_x\right) + Bg_{xx}) = 0, \tag{5.21}$$

$$\omega B - k_y k_E B_X + B\frac{B_u}{4\pi ne}\left(k_y B_X + k_z k_B B_{XX}\right) = 0. \tag{5.22}$$

Note that in (5.22) all variables depend only on X and all derivatives are with respect to X. It is tempting to interpret (5.22) as a consistence condition for k_y, k_z, k_E, k_B and $B = (X)$, while (5.21) may be interpreted as an equation for viable $g(x)$. However, at this stage using (5.21) and (5.22) to place restrictions on the model parameters is premature, given the number of approximations made to separate the first-order corrections. These two equations only show that there are no gross inconsistencies in the proposed model of the rippling.

Two-fluid hydrodynamics in the downstream region requires taking into account the non-gyrotropy of the ion distribution and its slow gyrotropization. It is more convenient to replace the two-fluid approach with the conservation laws together with the collisionless relaxation principles (Gedalin *et al.* 2015).

6. Implications for downstream collisionless relaxation

Upon crossing the ramp ions begin to gyrate. In a stationary planar shock the total downstream ion pressure p_{ij} is a function of the distance from the ramp L. The total pressure includes the dynamic pressure nmV_iV_j and the kinetic pressure P_{ij}, $p_{ij} = nmV_iV_j + P_{ij}$, where V_i is the bulk flow velocity. As a result of the kinematic collisionless

https://doi.org/10.1017/S0022377822000356 Published online by Cambridge University Press

relaxation, the kinetic pressure P_{ij} gradually gyrotropizes and further isotropizes, while the dynamic pressure tensor reduces to three components only: nmV_x^2; nmV_z^2 and nmV_xV_z. In a stationary planar shock the total downstream ion pressure depends on the distance x_d from the downstream edge of the ramp, $p_{ij} = p_{ij}(x_d)$. In the approximation of a small amplitude rippling this dependence may be replaced with the dependence on $x_n = x_d + a\psi(y, z, t)$. In a more general way, the ion distribution function becomes dependent on ψ. Therefore, all other moments, such as the bulk velocity vector, are also functions of ψ. For $\psi = \sin(k_y y + k_z z - \omega t)$ this would mean a spatially periodic pattern propagating along the shock front. Such a pattern should be easily observed in simulations but is difficult to identify even with four-spacecraft measurements. One immediate implication of the new dependence is that weak spatial and/or temporal averaging results in smearing out the peak values of the moments. In particular, the minimum value of averaged p_{xx} is larger than the minimum value of p_{xx} in the case if the shock were stationary and planar. Accordingly, the maximum value of averaged p_{xx} decreases. The conservation laws read

$$n_t + \sum_{j=x,y,z} (nV_j)_j = 0, \tag{6.1}$$

$$(nmV_i)_t + \sum_{j=x,y,z} (p_{ij} + \Pi_{ij})_j = 0, \tag{6.2}$$

$$\Pi_{ij} = \frac{1}{8\pi}(B^2\delta_{ij} - 2B_iB_j). \tag{6.3}$$

Averaging over y, z, t we arrive at the conservation laws in the form

$$\langle nV_x \rangle = \text{const.}, \tag{6.4}$$

$$\langle p_{ix} \rangle + \langle \Pi_{ix} \rangle = \text{const.}, \tag{6.5}$$

where $\langle \cdots \rangle$ means averaging. Smearing out the peak values of the pressure means a reduction of the amplitude of the downstream magnetic field oscillations. In this way rippling enhances kinematic collisionless relaxation. Figure 3 illustrates the dispersion of ion trajectories caused by the rippling. For this purpose figure 3(*b*) shows x versus v_x for an ion moving from upstream with the velocity of the flow, $\boldsymbol{v}_{\text{initial}} = (V_u, 0, 0)$, in the shock without rippling with the above chosen profile. Figure 3(*a*) shows x versus v_x for ions with $\boldsymbol{v}_{\text{initial}} = (V_u, 0, 0)$ starting at randomly chosen $0 < z < V_u/\Omega_u$ and the same x_{initial}. For figure 3(*a*) the shock is rippled with the parameters mentioned above but $k_y = 0$ and $\omega = 0$. The blue dotted line shows the magnetic field magnitudes corresponding to the positions x of all ions, independently of y and z.

Since the incident ions cross the ramp in different positions because of rippling, it can be expected that the downstream heating parameters, averaged over y, z and t, would differ from those which are achieved in a stationary planar shock with the same parameters. In order to compare the parallel and perpendicular heating in a rippled shock with its stationary counterpart, 40 000 initially Maxwellian distributed ions with $\beta_i = 0.2$ were traced across the shock in both cases and parallel and perpendicular temperatures were calculated well downstream of the transition region. The normalized upstream temperature in both cases is $T_u/m_pV_u^2 = 0.016$. The distributions behind the shock are strongly anisotropic. Without rippling the temperatures are $T_{d,\parallel}/m_pV_u^2 = 0.016$ and $T_{d,\perp}/m_pV_u^2 = 0.178$. No parallel heating occurs. With rippling we obtained $T_{d,\parallel}/m_pV_u^2 = 0.018$, $T_{d,\perp}/m_pV_u^2 = 0.182$, which means weak parallel heating and lower anisotropy.

https://doi.org/10.1017/S0022377822000356 Published online by Cambridge University Press

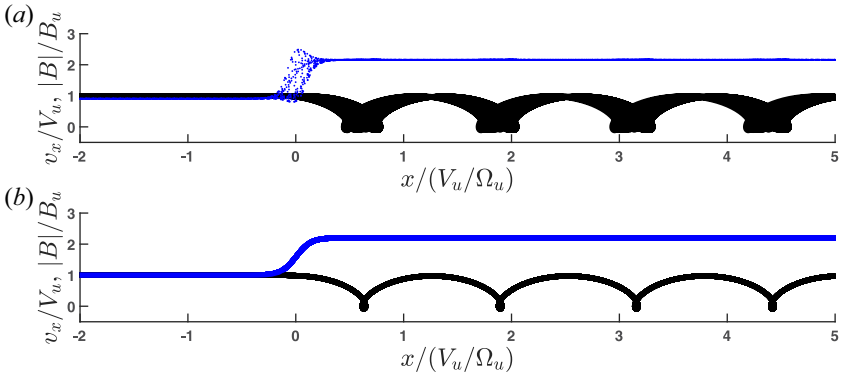

FIGURE 3. Trajectories, x versus v_x, for ions entering the shock with the velocity of the upstream flow at different initial z: (*a*) the rippled shock; (*b*) no rippling. The blue dotted line shows the magnetic field magnitudes corresponding to the positions x of all ions.

Corrections to the averaged conservation laws may be obtained by replacing

$$\partial_i = a\psi_i \partial_x, \quad i = t, y, z \tag{6.6}$$

which gives

$$\partial_x \left(nV_x + \sum_{i=t,y,z} a\psi_i n V_i \right) = 0, \tag{6.7}$$

$$\partial_x \left[a\psi_t nmV_i + p_{xx} + \Pi_{xx} + \sum_{j=y,z} a\psi_j (p_{ij} + \Pi_{ij}) \right] = 0. \tag{6.8}$$

Thus, for example, nV_x and $p_{xx} + \Pi_{xx}$ are no longer constant throughout the shock but the deviations are proportional to the small amplitude of the rippling.

The above analysis was done in the lowest-order approximation which describes the rippling as a simple shift of the position of the ramp of the kind $\Delta x = a\psi(y, z, t)$. Beyond this approximation, the maximum magnetic field and the cross-ramp potential also change with the shift, which further affects the ion motion and can be expected to cause more efficient relaxation. As a result, the spatial scale of the gyrotropization and isotropization downstream of the ramp should be smaller than the corresponding scale in a stationary planar shock. In the present study we model rippling with a monochromatic wave. Even multispacecraft observations provide information only about a small part of the shock surface. Simulations (Umeda & Daicho 2018; Omidi *et al.* 2021) show that rippling is only approximately monochromatic. Finite width of the spectrum would further enhance gyrotropization and isotropization by adding randomness in the gyrophases of the ion which are mixed at a fixed spatial position behind the ramp.

7. Discussion

At present, there is no theory of the rippling development, and we do not know what the rippling parameters should be and how they depend on the shock parameters, such as Mach number and the angle between the shock normal and the upstream magnetic field. Therefore, our study focused on the implications of a time-dependent rippling for the pattern of the electric and magnetic fields inside the ramp and in the upstream and

https://doi.org/10.1017/S0022377822000356 Published online by Cambridge University Press

downstream regions adjacent to the ramp, as well as for the ion motion and distributions in the rippled structure. It is clear that the functional dependence of the vector potential on the coordinates and time may be different from the model adopted in this study. Accordingly, the field profiles may differ in detail from those shown in the figures. However, the general conclusions about the deviations from the stationary planar fields are rather independent of the particular shape. Upstream and downstream whistlers diverging from the ramp may not propagate far from the shock, and possibly only traces of such whistlers with the footprints at the rippled ramp would be observed. The downstream pattern should be induced by the ion distributions following the rippling pattern, and the relaxation to thermal equilibrium should be faster because of the enhanced mixing. Waves which cross the shock and instabilities in the foreshock, foot and downstream region would affect the ion motion and also change the observed fields. Yet, we expect that the main effect would be produced by the macroscopic fields of the rippled shock front. All numerical illustrations in this study were done with a rather modest rippling and for shock parameters which essentially excluded ion reflection. In supercritical shocks, reflected ions play an important role in the formation of downstream distributions and contribute significantly to ion heating. Ion reflection will be also affected by the rippling. The effect may be expected to be stronger since a reflected ion crosses the ramp up to three times (Gedalin 1996*a*, 2016; Balikhin & Gedalin 2022). Detailed study of the ion motion and distributions in a supercritical rippled shock, together with the dependence on the rippling parameters, will be performed later.

8. Conclusions

We modelled rippling of the shock front as a monochromatic wave propagating along the shock front but localized within the ramp. Such rippling causes similar patterns in the fields inside and around the ramp. The most prominent observable changes of the fields inside the ramp are variations of the normal component of the magnetic field and of the motional component of the electric field. The rippling should cause whistlers diverging from the ramp. The whistlers should propagate obliquely to the shock normal and to the ambient magnetic field. The downstream magnetic field pattern should roughly follow the pattern of the rippling. The amplitude of the magnetic field oscillations should be smaller than in the stationary planar shock with the same parameters. Gyrotropization and isotropization should occur at smaller scales than what would happen in a stationary planar shock with the same shock parameters. Our conclusions can be verified with numerical simulations and used to determine the rippling parameters from observations. The objective of this study was to show that even weak rippling has clear effects on the observable fields and particle distributions in the shock front. We defer for future studies analysis of more realistic rippling in supercritical shocks with significant ion reflection.

Acknowledgements

Editor A.C. Bret thanks the referees for their advice in evaluating this article.

Funding

The work was partially supported by the European Union's Horizon 2020 research and innovation programme under grant agreement no. 101004131 (SHARP).

Declaration of interests

The authors report no conflict of interest.

https://doi.org/10.1017/S0022377822000356 Published online by Cambridge University Press

Appendix A

One has

$$B_z = \frac{\partial A_y}{\partial x} = \frac{\mathrm{d}A}{\mathrm{d}X}\left(\frac{\partial X}{\partial x}\right), \tag{A1}$$

$$B_x = -\frac{\partial A_y}{\partial z} + \frac{\partial A_z}{\partial y} = B_u\cos\theta - \frac{\mathrm{d}A}{\mathrm{d}X}\left(\frac{\partial X}{\partial z}\right) + k_B\frac{\mathrm{d}^2A}{\mathrm{d}X^2}\left(\frac{\partial X}{\partial y}\right), \tag{A2}$$

$$B_y = -\frac{\partial A_z}{\partial x} = -k_B\frac{\mathrm{d}^2A}{\mathrm{d}X^2}\left(\frac{\partial X}{\partial x}\right), \tag{A3}$$

$$E_x = -\frac{\partial \phi}{\partial x} = -k_E\frac{\mathrm{d}^2A}{\mathrm{d}X^2}\left(\frac{\partial X}{\partial x}\right), \tag{A4}$$

$$E_y = -\frac{\partial A_y}{\partial t} - \frac{\partial \phi}{\partial y} = V_uB_u\sin\theta - \frac{\mathrm{d}A}{\mathrm{d}X}\left(\frac{\partial X}{\partial t}\right) - k_E\frac{\mathrm{d}^2A}{\mathrm{d}X^2}\left(\frac{\partial X}{\partial y}\right), \tag{A5}$$

$$E_z = -\frac{\partial A_z}{\partial t} - \frac{\partial \phi}{\partial z} = -k_B\frac{\mathrm{d}^2A}{\mathrm{d}X^2}\left(\frac{\partial X}{\partial t}\right) - k_E\frac{\mathrm{d}^2A}{\mathrm{d}X^2}\left(\frac{\partial X}{\partial z}\right). \tag{A6}$$

Let

$$\frac{\mathrm{d}A}{\mathrm{d}X} = B_uB(X)\sin\theta \tag{A7}$$

then

$$B_z = B_u\sin\theta B(1+f_x), \tag{A8}$$

$$B_x = B_u\sin\theta\left(\cot\theta - Bf_z + k_BB_Xf_y\right), \tag{A9}$$

$$B_y = -k_BB_u\sin\theta B_X(1+f_x), \tag{A10}$$

$$E_x = -k_EB_u\sin\theta B_X(1+f_x), \tag{A11}$$

$$E_y = V_uB_u\sin\theta - B_u\sin\theta Bf_t - k_EB_u\sin\theta B_Xf_y, \tag{A12}$$

$$E_z = -B_u\sin\theta k_BB_Xf_t - k_EB_u\sin\theta B_Xf_z, \tag{A13}$$

$$\frac{\partial B_z}{\partial x} = B_u\sin\theta B_X(1+f_x)^2 + B_u\sin\theta Bf_{xx}, \tag{A14}$$

$$\frac{\partial B_z}{\partial y} = B_u\sin\theta B_X(1+f_x)f_y + B_u\sin\theta Bf_{xy}, \tag{A15}$$

$$\frac{\partial B_x}{\partial y} = -B_u\sin\theta Bf_{zy} - B_u\sin\theta B_Xf_yf_z + k_BB_u\sin\theta B_{XX}f_y^2 + k_BB_u\sin\theta B_Xf_{yy}, \tag{A16}$$

$$\frac{\partial B_x}{\partial z} = -B_u\sin\theta Bf_{zz} - B_u\sin\theta B_Xf_z^2 + k_BB_u\sin\theta B_{XX}f_yf_z + k_BB_u\sin\theta B_Xf_{yz}, \tag{A17}$$

$$\frac{\partial B_y}{\partial x} = -k_BB_u\sin\theta B_{XX}(1+f_x)^2 - k_BB_u\sin\theta B_Xf_{xx}, \tag{A18}$$

$$\frac{\partial B_y}{\partial z} = -k_BB_u\sin\theta B_{XX}(1+f_x)f_z - k_BB_u\sin\theta B_Xf_{xz}. \tag{A19}$$

https://doi.org/10.1017/S0022377822000356 Published online by Cambridge University Press

Here

$$B_X = \frac{\mathrm{d}B}{\mathrm{d}X}, \quad B_{XX} = \frac{\mathrm{d}^2B}{\mathrm{d}X^2}, \tag{A 20a,b}$$

$$g' = \frac{\mathrm{d}g}{\mathrm{d}x}, \quad f_x = -a\psi g', \quad f_\xi = -ag\psi_\xi, \quad \xi = y, z, t, \tag{A 21a–d}$$

$$\partial_x = (1 + f_x)\frac{\mathrm{d}}{\mathrm{d}X}, \quad \partial_\xi = f_\xi \frac{\mathrm{d}}{\mathrm{d}X} \tag{A 22a,b}$$

are all localized. The normalized coefficients remain the same as in one-dimensional stationary case (see (2.6) and (2.7)),

$$k_E = \frac{s_{\mathrm{NIF}}}{2(R-1)}, \tag{A23}$$

$$k_B = \frac{(s_{HT} - s_{\mathrm{NIF}})\cos\theta}{2\sin\theta\,(R-1)}. \tag{A24}$$

Each differentiation of X with respect to x, y, z, t adds a small multiplier. The derivatives $f_t, f_x, f_y, f_z, f_{xx}$ are of the first order. The terms $f_x^2, f_y^2, f_z^2, f_{xy}, f_{xz}, f_{yy}, f_{yz}, f_{zz}$ are of the second order. We shall restrict ourselves with the first order only. Meanwhile we do not make assumptions about k_B.

REFERENCES

Axford, W.I., Leer, E. & Skadron, G. 1977 The acceleration of cosmic rays by shock waves. In *International Cosmic Ray Conference, 15th, Plovdiv, Bulgaria, August 13–26, 1977, Conference Papers. Volume 11. (A79-44583 19-93) Sofia, B'lgarska Akademiia na Naukite, 1978, pp. 132–137*, pp. 13–26. Plovdiv.

Bale, S.D., Balikhin, M.A., Horbury, T.S., Krasnoselskikh, V.V., Kucharek, H., Möbius, E., Walker, S.N., Balogh, A., Burgess, D., Lembège, B., *et al.* 2005 Quasi-perpendicular shock structure and processes. *Space Sci. Rev*. **118** (1), 161–203.

Balikhin, M.A., Zhang, T.L., Gedalin, M., Ganushkina, N.Y. & Pope, S.A. 2008 Venus express observes a new type of shock with pure kinematic relaxation. *Geophys. Res. Lett*. **35**, L01103.

Balikhin, M. & Gedalin, M. 2022 Collisionless shocks in the heliosphere: foot width revisited. *Astrophys. J* **925**, 90.

Bell, A.R. 1978 The acceleration of cosmic rays in shock fronts. I. *Mon. Not. R. Astron. Soc*. **182**, 147–156.

Blandford, R.D. & Ostriker, J.P. 1978 Particle acceleration by astrophysical shocks. *Astrophys. J*. **221**, L29–L32.

Blandford, R. & Eichler, D. 1987 Particle acceleration at astrophysical shocks: a theory of cosmic ray origin. *Phys. Rep*. **154** (1), 1–75.

Burgess, D., Hellinger, P., Gingell, I. & Trávníček, P.M. 2016 Microstructure in two- and three-dimensional hybrid simulations of perpendicular collisionless shocks. *J. Plasma Phys*. **82** (4), 905820401.

Burgess, D. & Scholer, M. 2007 Shock front instability associated with reflected ions at the perpendicular shock. *Phys. Plasmas* **14** (1), 012108.

Drury, L.O. 1983 An introduction to the theory of diffusive shock acceleration of energetic particles in tenuous plasmas. *Rep. Prog. Phys*. **46**, 973–1027.

Farris, M., Russell, C. & Thomsen, M. 1993 Magnetic structure of the low beta, quasi-perpendicular shock. *J. Geophys. Res*. **98**, 15285–15294.

Gedalin, M. 1996*a* Ion reflection at the shock front revisited. *J. Geophys. Res*. **101** (A), 4871–4878.

Gedalin, M. 1996*b* Noncoplanar magnetic field in the collisionless shock front. *J. Geophys. Res*. **101** (A5), 11153–11156.

https://doi.org/10.1017/S0022377822000356 Published online by Cambridge University Press

GEDALIN, M. 1997 Ion heating in oblique low-Mach number shocks. *Geophys. Res. Lett*. **24** (2), 2511–2514.

GEDALIN, M. 1998 Low-frequency nonlinear stationary waves and fast shocks: hydrodynamical description. *Phys. Plasmas* **5** (1), 127–132.

GEDALIN, M. 2016 Transmitted, reflected, quasi-reflected, and multiply reflected ions in low-Mach number shocks. *J. Geophys. Res*. **121** (1), 10.

GEDALIN, M. 2021 Shock heating of directly transmitted ions. *Astrophys. J*. **912** (2), 82.

GEDALIN, M., FRIEDMAN, Y. & BALIKHIN, M. 2015 Collisionless relaxation of downstream ion distributions in low-Mach number shocks. *Phys. Plasmas* **22**, 072301.

GEDALIN, M., GOLBRAIKH, E., RUSSELL, C.T. & DIMMOCK, A.P. 2022 Theory helps observations: determination of the shock mach number and scales from magnetic measurements. *Front. Phys*. **10**, 11.

GEDALIN, M., POGORELOV, N.V. & ROYTERSHTEYN, V. 2021 Boundary conditions at the heliospheric termination shock with pickup ions. *Astrophys. J*. **916** (1), 57.

GINGELL, I., SCHWARTZ, S.J., BURGESS, D., JOHLANDER, A., RUSSELL, C.T., BURCH, J.L., ERGUN, R.E., FUSELIER, S., GERSHMAN, D.J., GILES, B.L., *et al.* 2017 MMS observations and hybrid simulations of surface ripples at a marginally quasi-parallel shock. *J. Geophys. Res*. **77** (16), 736–11017.

GOODRICH, C.C. & SCUDDER, J.D. 1984 The adiabatic energy change of plasma electrons and the frame dependence of the cross-shock potential at collisionless magnetosonic shock waves. *J. Geophys. Res*. **89**, 6654–6662.

GOSLING, J.T., WINSKE, D. & THOMSEN, M.F. 1988 Noncoplanar magnetic fields at collisionless shocks: a test of a new approach. *J. Geophys. Res*. **93** (A4), 2735.

GREENSTADT, E.W., SCARF, F.L., RUSSELL, C.T., GOSLING, J.T., BAME, S.J., PASCHMANN, G., PARKS, G.K., ANDERSON, K.A., ANDERSON, R.R. & GURNETT, D.A. 1980 A macroscopic profile of the typical quasi-perpendicular bow shock – ISEE 1 and 2. *J. Geophys. Res*. **85**, 2124–2130.

HAO, Y., LU, Q., GAO, X. & WANG, S. 2016 Ion dynamics at a rippled quasi-parallel shock: 2d hybrid simulations. *Astrophys. J*. **823** (1), 7.

HOBARA, Y., BALIKHIN, M., KRASNOSELSKIKH, V., GEDALIN, M. & YAMAGISHI, H. 2010 Statistical study of the quasi-perpendicular shock ramp widths. *J. Geophys. Res*. **115** (A11), 11106.

HULL, A.J., MUSCHIETTI, L., OKA, M., LARSON, D.E., MOZER, F.S., CHASTON, C.C., BONNELL, J.W. & HOSPODARSKY, G.B. 2012 Multiscale whistler waves within Earth's perpendicular bow shock. *J. Geophys. Res*. **117** (A), A12104.

JOHLANDER, A., SCHWARTZ, S.J., VAIVADS, A., KHOTYAINTSEV, Y.V., GINGELL, I., PENG, I.B., MARKIDIS, S., LINDQVIST, P.A., ERGUN, R.E., MARKLUND, G.T., *et al.* 2016 Rippled quasiperpendicular shock observed by the magnetospheric multiscale spacecraft. *Phys. Rev. Lett*. **117** (16), 165101.

JOHLANDER, A., VAIVADS, A., KHOTYAINTSEV, Y.V., GINGELL, I., SCHWARTZ, S.J., GILES, B.L., TORBERT, R.B. & RUSSELL, C.T. 2018 Shock ripples observed by the MMS spacecraft: ion reflection and dispersive properties. *Plasma Phys. Control. Fusion* **60** (12), 125006.

JOKIPII, J.R. 1982 Particle drift, diffusion, and acceleration at shocks. *Astrophys. J*. **255**, 716–720.

JONES, F.C. & ELLISON, D.C. 1987 Noncoplanar magnetic fields, shock potentials, and ion deflection. *J. Geophys. Res*. **92** (A10), 11205.

JONES, T.W. 2011 Particle acceleration at shocks: insights from supernova remnant shocks. *J. Astrophys. Astron*. **32**, 427–435.

KRASNOSELSKIKH, V., BALIKHIN, M., WALKER, S.N., SCHWARTZ, S., SUNDKVIST, D., LOBZIN, V., GEDALIN, M., BALE, S.D., MOZER, F., SOUCEK, J., *et al.* 2013 The dynamic quasiperpendicular shock: cluster discoveries. *Space Sci. Rev*. **178** (2), 535–598.

KRYMSKII, G.F. 1977 A regular mechanism for the acceleration of charged particles on the front of a shock wave. *Sov. Phys. Dokl*. **22**, 327.

LOBZIN, V.V., KRASNOSELSKIKH, V.V., MUSATENKO, K. & DUDOK DE WIT, T. 2008 On nonstationarity and rippling of the quasiperpendicular zone of the Earth bow shock: cluster observations. *Ann. Geophys*. **26** (9), 2899–2910.

LOWE, R.E. & BURGESS, D. 2003 The properties and causes of rippling in quasi-perpendicular collisionless shock fronts. *Ann. Geophys*. **21** (3), 671–679.

MADANIAN, H., DESAI, M.I., SCHWARTZ, S.J., WILSON, L.B., FUSELIER, S.A., BURCH, J.L., LE CONTEL, O., TURNER, D.L., OGASAWARA, K., BROSIUS, A.L., *et al.* 2021 The dynamics of a high Mach number quasi-perpendicular shock: MMS observations. *Astrophys. J*. **908** (1), 40.

MASTERS, A., STAWARZ, L., FUJIMOTO, M., SCHWARTZ, S.J., SERGIS, N., THOMSEN, M.F., RETINÒ, A., HASEGAWA, H., ZIEGER, B., LEWIS, G.R., *et al.* 2013 In situ observations of high-Mach number collisionless shocks in space plasmas. *Plasma Phys. Control. Fusion* **55** (12), 124035.

MELLOTT, M.M. & GREENSTADT, E.W. 1984 The structure of oblique subcritical bow shocks – ISEE 1 and 2 observations. *J. Geophys. Res*. **89**, 2151–2161.

MOULLARD, O., BURGESS, D., HORBURY, T.S. & LUCEK, E.A. 2006 Ripples observed on the surface of the Earth's quasi-perpendicular bow shock. *J. Geophys. Res*. **111** (A), A09113.

NEWBURY, J.A. & RUSSELL, C.T. 1996 Observations of a very thin collisionless shock. *Geophys. Res. Lett*. **23** (7), 781–784.

OFMAN, L. & GEDALIN, M. 2013 Rippled quasi-perpendicular collisionless shocks: local and global normals. *J. Geophys. Res*. **118** (1), 5999–6006.

OMIDI, N., DESAI, M., RUSSELL, C.T. & HOWES, G.G. 2021 High Mach number quasi-perpendicular shocks: spatial versus temporal structure. *J. Geophys. Res*. **126** (9), e2021JA029287.

RAMÍREZ VÉLEZ, J.C., BLANCO-CANO, X., AGUILAR-RODRIGUEZ, E., RUSSELL, C.T., KAJDIČ, P., JIAN, L.K. & LUHMANN, J.G. 2012 Whistler waves associated with weak interplanetary shocks. *J. Geophys. Res*. **117** (A), A11103.

RAYMOND, J.C. 2018 Shock waves in supernova ejecta. *Space Sci. Rev*. **214** (1), 1–25.

REYNOLDS, S. 2004 Microphysics of shock acceleration from observations of X-ray synchrotron emission from supernova remnants. *Adv. Space Res*. **33** (4), 461–465.

RIQUELME, M.A. & SPITKOVSKY, A. 2011 Electron injection by whistler waves in non-relativistic shocks. *Astrophys. J*. **733** (1), 63.

RUSSELL, C., HOPPE, M., LIVESEY, W. & GOSLING, J. 1982 Isee-1 and-2 observations of laminar bow shocks- velocity and thickness. *Geophys. Res. Lett*. **9**, 1171.

SULAIMAN, A.H., MASTERS, A., DOUGHERTY, M.K., BURGESS, D., FUJIMOTO, M. & HOSPODARSKY, G.B. 2015 Quasiperpendicular high Mach number shocks. *Phys. Rev. Lett*. **115** (12), 125001.

TOPTYGHIN, I.N. 1980 Acceleration of particles by shocks in a cosmic plasma. *Space Sci. Rev*. **26**, 157–213.

UMEDA, T. & DAICHO, Y. 2018 Periodic self-reformation of rippled perpendicular collisionless shocks in two dimensions. *Ann. Geophys*. **36** (4), 1047–1055.

VASILEV, V.N., TOPTYGIN, I.N. & CHIRKOV, A.G. 1978 Interaction between energetic particles and a shock front in a turbulent medium. *Geomagn. Aeron*. **18**, 415–422.

VINK, J. 2004*a* A review of X-ray observations of supernova remnants. *Nucl. Phys.* B **132**, 21–30.

VINK, J. 2004*b* Shocks and particle acceleration in supernova remnants: observational features. *Adv. Space Res*. **33** (4), 356–365.

VINK, J. 2020 *Physics and Evolution of Supernova Remnants*. Springer International Publishing.

WILSON III, L.B., KOVAL, A., SZABO, A., STEVENS, M.L., KASPER, J.C., CATTELL, C.A. & KRASNOSELSKIKH, V.V. 2017 Revisiting the structure of low-Mach number, low-beta, quasi-perpendicular shocks. *J. Geophys. Res*. **81** (4), 2097–9133.

WILSON, L.B.I., CATTELL, C.A., KELLOGG, P.J., GOETZ, K., KERSTEN, K., KASPER, J.C., SZABO, A. & MEZIANE, K. 2009 Low-frequency whistler waves and shocklets observed at quasi-perpendicular interplanetary shocks. *J. Geophys. Res*. **114** (A), A10106.

WILSON, L.B.I., KOVAL, A., SZABO, A., BRENEMAN, A., CATTELL, C.A., GOETZ, K., KELLOGG, P.J., KERSTEN, K., KASPER, J.C., MARUCA, B.A., *et al.* 2012 Observations of electromagnetic whistler precursors at supercritical interplanetary shocks. *Geophys. Res. Lett*. **39** (8), L08109.

YUAN, X., CAIRNS, I.H., TRICHTCHENKO, L., RANKIN, R. & DANSKIN, D.W. 2009 Confirmation of quasi-perpendicular shock reformation in two-dimensional hybrid simulations. *Geophys. Res. Lett*. **36** (5), L05103.